

# Laboratory experiments simulating a coastal river inflow

By ALEXANDER R. HORNER-DEVINE<sup>1</sup>†,  
DEREK A. FONG<sup>1</sup>, STEPHEN G. MONISMITH<sup>1</sup>  
AND TONY MAXWORTHY<sup>2</sup>

<sup>1</sup>Environmental Fluid Mechanics Laboratory, Department of Civil and Environmental Engineering,  
Stanford University, Stanford, CA 94305-4020, USA

<sup>2</sup>Department of Aerospace and Mechanical Engineering, University of Southern California,  
Los Angeles, CA 90089, USA

(Received 9 September 2004 and in revised form 27 October 2005)

The dynamics of buoyant water entering a rotating basin are studied using a series of laboratory experiments designed to elucidate the alongshore transport mechanisms in river plumes. Inflowing water, which is discharged perpendicular to the tank wall, is observed to form a growing anticyclonic bulge and a coastal current downstream of the bulge. Detailed simultaneous measurements of the velocity and buoyancy fields in the plume confirm that the bulge momentum is in a gradient–wind balance and the coastal current is geostrophic. The growth of the bulge and accumulation of fluid within it coincides with a reduction in coastal current transport to approximately 50% of the inflow discharge. The bulge is characterized by a depth scale,  $h$ , which is proportional to the geostrophic depth,  $h_g$ , and two time-dependent horizontal length scales,  $y_c$ , the displacement of the bulge centre from the wall, and  $r_b$ , the effective radius of the bulge. These two length scales are proportional to the inertial radius,  $L_i$ , and the local Rossby radius,  $L_b$ , respectively. When  $r_b \gg y_c$ , the bulge is held tightly to the wall, and a relatively large fraction of the inflow discharge is forced into the coastal current. For plumes with  $y_c$  approaching  $r_b$ , the bulge is further from the wall, and the coastal current flux is reduced. Once  $y_c/r_b > 0.7$ , the bulge separates from the wall causing flow into the coastal current to cease and the bulge to become unstable. In this state, the bulge periodically detaches from and re-attaches to the wall, resulting in pulsing transport in the coastal current. Scaling of the bulge growth based on  $h_g$ ,  $L_i$  and  $L_b$  predicts that it will increase as  $Ro^{1/4}$ , where  $Ro$  is the inflow Rossby number. The bulge growth, inferred from direct measurements of the coastal current transport, is proportional to  $Ro^{0.32}$  and agrees with the predicted dependence within the experimental error.

---

## 1. Introduction

River inflows and their associated buoyant plumes are a major source of nutrients, sediments and contaminants to coastal waters, where they support diverse and productive ecosystems. Recently, considerable effort has been made to understand the circulation within river plumes in order to determine the transport and dispersal of

† Present address: Department of Civil and Environmental Engineering, University of Washington, Seattle, WA, 98195-2700, USA.

river-borne matter in the coastal zone. The dynamical behaviour of the simplest model inflow, a buoyant discharge into a quiescent rotating basin, is not yet fully understood, however. In particular, the rate at which river water is transported away from the mouth is not known. In the present work, a simple model inflow is generated in the laboratory and the dynamics and transport mechanisms of the plume are described.

A number of laboratory studies relevant to river inflows have examined the dynamics of buoyant rotating gravity currents, such as those that form downstream (in the sense of Kelvin wave propagation) of buoyant discharges (e.g. Stern, Whitehead & Hua 1982; Griffiths & Hopfinger 1983; Whitehead & Chapman 1986; Lentz & Helfrich 2002; Avicola & Huq 2002). In these studies, a coastally trapped gravity current is generated by discharging buoyant water parallel to the coastal wall, using either a constant source or a ‘dam break’. It is clear from recent laboratory studies, however, that inflows initiated perpendicular to the coastal wall are fundamentally different from those initiated parallel to it (Horner *et al.* 2000; Horner-Devine 2003; Avicola & Huq 2003*b*) and that the parallel discharge case may not accurately represent the circulation in river plumes, especially near the mouth of the river. This finding is consistent with many numerical modelling studies of river plumes (e.g. Chao & Boicourt 1986; Oey & Mellor 1993; Kourafalou *et al.* 1996; Fong & Geyer 2002), laboratory studies (e.g. Whitehead & Miller 1979; Bormans & Garrett 1989; Avicola & Huq 2003) and analytical studies (Nof & Pichevin 2001), which consider perpendicular inflows. In these studies, buoyant inflowing water is found to form an anticyclonic vortex, or bulge, immediately downstream of the inflow and a coastal current further downstream. While the coastal current width is of the order of the Rossby deformation radius, the bulge is unsteady and grows to many times the Rossby radius. Evidence of a bulge is observed in satellite images and field studies of the Niagara (Masse & Murthy 1992) and the Columbia (Hickey *et al.* 1998) river plumes. According to Fong & Geyer (2002), the bulge unsteadiness reduces the flux of river water into the coastal current to 25–75 % of the inflow discharge. Such a reduction in the alongshore flux modifies the plume circulation in the near and far field, since the width (Lentz & Helfrich 2002; Avicola & Huq 2003*a*) and alongshore penetration distance (Garvine 1999) of the coastal current depend on the flux of buoyant water at the head of the current.

### 1.1. Background

Large-scale buoyant coastal plumes are typically assumed to be in cross-shore geostrophic balance and to have widths that scale with the Rossby radius  $L_r = (g'h)^{1/2} f^{-1}$ , where  $h$  is the buoyant-layer thickness,  $f$  is the Coriolis frequency and  $g' = (\rho_o - \rho_i)\rho_o^{-1}$  is the reduced gravity based on the ambient and inflow densities,  $\rho_o$  and  $\rho_i$ , respectively (Garvine 1995). The bulge region, however, is characterized by relatively strong anticyclonic vorticity, and therefore centrifugal acceleration is likely to be important in addition to the geostrophic terms. In general, inclusion of the centrifugal term introduces a second length scale, the inertial radius  $L_i = Uf^{-1}$ , where  $U = Q(HW)^{-1}$  is the mean volumetric inflow velocity based on the inflow discharge  $Q$ , thickness  $H$  and width  $W$ . Flows in which the centrifugal and Coriolis accelerations balance the pressure gradient are said to be in gradient–wind balance,

$$\frac{v_\theta^2}{r} + fv_\theta = g' \frac{\partial h}{\partial r}. \quad (1.1)$$

This balance is referred to as either a *gradient–wind* or a *cyclostrophic* balance in the literature. We will use the term *gradient–wind*, since it is used in a number of

standard texts (e.g. Gill 1982; Holton 1972) and since *cyclostrophic* is also commonly used to refer to the two-way balance between centrifugal acceleration and pressure gradient. In this formulation,  $v_\theta$  is the depth-averaged orbital velocity,  $r$  is the radial coordinate relative to the centre of the bulge circulation and  $h$  is the plume thickness. Yankovsky & Chapman (1997) hypothesize that the bulge is in gradient–wind balance. They derive an independent length scale based on the gradient–wind balance and show agreement with the widths of a number of naturally occurring plumes.

## 1.2. Previous experiments

A number of laboratory experiments have modelled the analogous problem of ocean inflows such as the Tsugaru warm gyre in the Western Pacific Ocean and the Alboran gyre in the Western Mediterranean basin (Whitehead & Miller 1979; Kawasaki & Sugimoto 1984; Bormans & Garrett 1989; Gleizon, Chabert D’Hieres & Renouard 1996). These laboratory experiments all consisted of exchange flows between two basins of different density on a rotating table. Field observations of the Tsugaru inflow (Colon 1983) and the Alboran gyre (Lanoix 1974) indicate that both form buoyant anticyclonic lenses similar to the bulge under certain conditions. The laboratory experiments were primarily concerned with determining the conditions under which the gyre did or did not form.

Whitehead & Miller (1979) and Bormans & Garrett (1989) both reported that a growing anticyclonic gyre formed when the radius of curvature,  $R_w$ , of the inflow channel corner was less than the radius of curvature of the inflowing buoyant fluid. Experiments in which a sharp exit corner was used typically resulted in the formation of a growing gyre. Whitehead & Miller (1979) found that the width of the gyre increased as the square root of time, consistent with Fong & Geyer (2002), and scaled with the Rossby radius,  $L_D = (g'D)^{1/2} f^{-1}$ , where  $D$  is the total depth of the water. As outlined in Bormans & Garrett (1989), however, the experiments of Whitehead & Miller (1979) were limited to the exit Froude number,  $Fr = u(g'h)^{-1/2} \leq 1$ , where  $h$  is the upper-layer depth. In this case, Bormans & Garrett (1989) argue that  $L_D R_w^{-1}$  reduces to  $u(fR_w)^{-1}$  and the radius of curvature of the inflowing water is set instead by the inertial radius. They propose that  $u(fR_w)^{-1} > 1$  is a more general criterion for gyre formation when  $Fr$  is not necessarily equal to 1. The results of their experiments support this criterion.

Gleizon *et al.* (1996) used a two-basin approach similar to the previous experiments, except that they discharged the buoyant fluid into the western basin and withdrew it from the eastern basin at a constant rate in order to control the flow rate through the channel. They showed that two gyres, which were identical except for their discharge, looked qualitatively similar if one was shifted in time by  $\tau(Q)$ , a temporal shift that is only a function of the inflow rate  $Q$ .

Klinger (1994) and Sadoux *et al.* (2000) both examined the role of capes in generating oceanic gyres from geostrophic coastal currents. In contrast to Whitehead & Miller (1979) and Fong & Geyer (2002), these studies found that the width of the gyre increased linearly in time. Klinger (1994) considered the dynamical significance of the lower-layer return flow in currents generated with an exchange flow. He found that a gyre generated with an exchange flow was accompanied by a corresponding gyre with the opposite sense of rotation in the lower layer. In many of his experiments, this cyclonic gyre paired with the upper-layer anticyclonic gyre and the two self-advected away from the wall. In experiments with a simple constant source inflow such as those described in the current study, no lower-layer cyclone formed and the upper-layer anticyclonic gyre was held against the wall.

Avicola & Huq (2003a) examined the characteristics of the bulge in laboratory experiments with a constant buoyant source that discharged via a rectangular bay into a quiescent flat-bottomed tank. They varied the angle that the bay made with the coast and the outlet radius of curvature of the bay, as well as  $f$  and  $g'$ . The bulge formed only for experiments with a high inflow angle. In these runs, they observed that the coastal current was narrower and propagated along the coast more slowly than in runs where no bulge formed. They showed that the reduction in the alongshore propagation speed and width of the coastal current was consistent with a growing bulge that accumulated 60–70% of the freshwater discharge. They found that the bulge width scaled with the local Rossby radius,  $L_b$ , and increased as  $t^{2/5}$ , and that the bulge depth scaled with a geostrophic depth scale,  $h_b$ , and increased as  $t^{1/5}$ . However, they did not vary the inflow discharge  $Q$  significantly, making it difficult to determine the role of the inertial radius. In a companion paper, Avicola & Huq (2003b) considered the role of the inflow angle. In this case, they found that the cross-shore scale of the bulge was set by the inertial radius.

All of these studies scaled the gyre width by either the Rossby radius or the inertial radius. However, there is no consensus among the different studies. As indicated by Bormans & Garrett (1989), this ambiguity is related to the fact that most experiments were carried out with  $Fr \simeq 1$ . Although this is a realistic parameter range for naturally occurring buoyant inflows, the experiments presented here demonstrate that deviation from a critical  $Fr$  over a relatively small range results in a significant change in the plume behaviour.

Furthermore, the above studies leave an important question unanswered. What determines how far the bulge is displaced from the coast? Nof (1988) presented a conceptual model of eddy–wall interaction that was later applied to the bulge by Fong & Geyer (2002). The eddy, or bulge, is modelled as a circle with one side clipped by the coast, and the discharge from the eddy depends on the fraction that intersects the coast. If only one scale is used to describe the bulge, as in the laboratory studies outlined above, the distance from the bulge centre to the coast is equal to the bulge radius, the bulge does not intersect the coast and no fluid is discharged into the coastal current. In all of the previously cited laboratory studies, however, the distance from the wall to the bulge centre is less than its radius and some buoyant fluid is discharged into the coastal current. A second length scale is required, therefore, to define the bulge geometry that fully characterizes the dynamics of the bulge and its relationship to the alongshore transport in the coastal current.

We present the results from a series of laboratory experiments designed to identify the scales relevant to bulge growth and to relate them to the reduction in alongshore transport in the plume. When the full experimental parameter range is spanned, we find that both the inertial radius and the Rossby radius emerge as important scales in the evolution of the bulge. In particular, both the bulge growth and alongshore transport depend on the ratio of these two scales,  $L^*$ .

### 1.3. Present experiments

For each experiment, buoyant water was introduced at a constant volumetric flow rate  $Q$  into a quiescent rotating tank using a simple rectangular source of width  $W$  and height  $H$ . The velocity and density fields in the resulting plume were measured with high spatial and temporal resolution in order to determine the scales of the flow as well as the flux of buoyant water in the coastal current. The simple rectangular source allows direct specification of the inflow Froude number and is a reasonable model of many river inflows for which there is no significant return flow in the lower

layer. It may not, however, be an accurate model of ocean inflows such as the Alboran gyre, in which a significant return flow exists in the lower layer, nor wide-mouthed estuaries where the inflow may be non-uniform (e.g. Garvine 2001).

### 1.3.1. Scales

The dynamics of the bulge and the corresponding transport in the coastal current were measured for a range of independent inflow parameters. In order to separate the buoyant and rotational dynamics, plumes are characterized by the inflow Rossby,  $Ro = U(fW)^{-1}$ , and Froude,  $Fr = U(g'H)^{-1/2}$ , numbers. Here,  $f = 4\pi T^{-1}$ ,  $T$  is the table rotation period and  $U = Q(WH)^{-1}$ . The same inflow parameters form four independent length scales that are relevant to this study: the inflow Rossby deformation radius, the inertial radius, the geostrophic bulge depth and the bulge Rossby radius. These are given by,

$$L_r = \frac{(g'H)^{1/2}}{f}, \quad L_i = \frac{U}{f}, \quad h_g = \left(\frac{2Qf}{g'}\right)^{1/2}, \quad L_b = \left(\frac{2Qg'}{f^3}\right)^{1/4}, \quad (1.2a-d)$$

respectively. The third scale,  $h_g$ , is the maximum depth in a geostrophic current with an alongshore flux equal to  $Q$  (Fong 1998; Lentz & Helfrich 2002) and the fourth scale,  $L_b$ , is the Rossby deformation radius based on the bulge depth scale  $h_g$ . Avicola & Huq (2003a) found that  $h_g$  and  $L_b$  described the bulge depth and width, respectively.

The gradient–wind momentum balance expressed by (1.1) involves a combination of both inertial and baroclinic dynamics. Thus, the inertial radius and Rossby radius are expected to emerge in the description of the plume dynamics. In (1.2b), the inertial radius is defined in terms of the inflow velocity,  $U$ , since, in a river-forced system, the inertia will be set by the inflow momentum. Once the bulge becomes very large, however, the relative influence of the inflow momentum will decrease and the bulge momentum will approach a geostrophic balance.

The two proposed scales  $L_i$  and  $L_b$  can be combined to form a new dimensionless parameter,

$$L^* = \frac{L_i}{L_b},$$

which describes the relative importance of the inflow momentum to the dynamics of the bulge.  $L^*$  is a function of independent inflow parameters and is related to the inflow Rossby and Froude numbers according to  $L^* = 2^{-1/4} Fr^{1/2} Ro^{1/4}$ . Since the scale of the bulge sets its volumetric capacity,  $L^*$  is also expected to determine the fractions of inflow discharge that are retained in the bulge and discharged into the coastal current. The dependences of the bulge evolution on  $L_i$  and  $L_b$  are determined separately in the present experiments in order to elucidate the dynamic significance of  $L^*$ . The alongshore transport is then measured over a range of  $Ro$  and  $Fr$  to investigate the dependence of the coastal current flux on  $L^*$ .

### 1.4. Experimental set-up

The experiments were conducted in an annular water tank set on a rotating table in the Environmental Fluid Mechanics Laboratory at Stanford University. The inner and outer tank walls are Plexiglas and have 92 cm and 22 cm radii, respectively, and the total tank depth is 24 cm. A 120 cm wall across one side forms the coastal wall (figure 1).

The source of the buoyant water is a 120 l constant head tank located above the level of the rotating table. Source water passes onto the table by means of a water slip ring. To create the inflow, the water is introduced into the tank through a diffuser

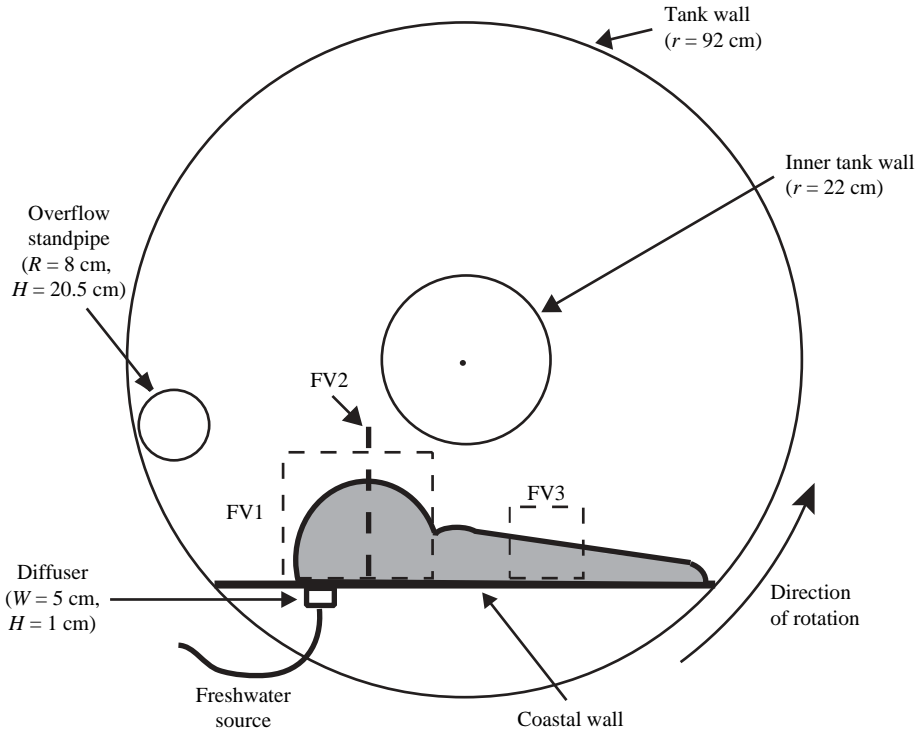


FIGURE 1. Schematic of the rotating table from above showing the camera field of view for the three measurement sections. FV1 is the camera field of view for the horizontal section through the bulge. For these experiments the camera is directly above the field of view looking down. FV2 is the plane of the laser sheet in the vertical bulge section. The plane is perpendicular to the figure, and it is viewed from the left-hand side by the camera. FV3 is the field of view in the angled coastal current section. In these experiments, the sheet is  $15^\circ$  to the horizontal, so that it intersects the surface on the right-hand side of the field of view and is submerged on the left-hand side. The camera is also inclined so that the entire field of view is in focus.

chamber attached to a 1 cm deep by 5 cm wide slot in the coastal wall at the level of the ambient water surface.

The velocity and buoyancy fields are measured simultaneously in a section of the flow using a combined digital particle image velocimetry (DPIV) and planar laser induced fluorescence (PLIF) technique developed by Cowen, Chang & Liao (2001). The technique involves acquiring a sequence of image triples with a digital camera that is fitted with a wavelength cut-off filter. The first two images in each triple are illuminated using a YAG laser, which has a wavelength higher than the cut-off wavelength so that light reflected off seed particles in the flow passes the filter. These image pairs are processed using a DPIV code developed by Cowen (e.g. Cowen *et al.* 2001) to obtain highly resolved velocity fields. The third image in the triple is illuminated using an argon ion laser sheet and processed using the PLIF technique (e.g. Crimaldi & Koseff 2001). The source is differentially dyed with fluorescein relative to the ambient water. The buoyancy field is calculated based on the fluorescent light emission from the dye. The combined DPIV/PLIF technique requires that laser sheets from both the YAG and argon ion lasers be formed in the rotating frame of reference. This is accomplished by combining the laser beams below the rotating table and directing

them vertically through an axial hole in the table. The beams are then steered horizontally through a cylindrical lens using a mirror on the rotating table.

We modified the DPIV/PLIF technique to measure the alongshore transport of buoyant fluid in the coastal current. Computing this flux requires measurement of density and alongshore velocities in a vertical slice perpendicular to the coastal wall. Measurements of alongshore displacement, however, are not possible in a laser sheet oriented perpendicular to the primary direction of fluid motion with only one camera. In order to circumvent this problem, we angled the laser sheet ( $\theta_s = 15^\circ$ ) relative to the horizontal. Since the sheet has a finite thickness ( $\simeq 1.5$  mm), particles that are displaced horizontally stay in the sheet and have a measurable displacement in the angled plane of the sheet. The resolved displacements are corrected to account for the sheet angle and projected onto a vertical plane. This technique was used to measure a prescribed flux to within 5% in a set of validation experiments (Horner-Devine 2003). The experimental conditions were carefully controlled to avoid or compensate for the effects of variations in index of refraction, differences in surface tension, photobleaching and pH sensitivity of the fluorescein dye, differential heating of the ambient tank fluid and wind resulting from the table rotation. The details of the experimental procedures are explained in greater detail in Horner-Devine (2003).

We conducted four separate sets of experiments. In the first set, velocity and buoyancy were measured in a near-surface horizontal section of the entire plume. In order to obtain a description of the entire plume evolution, two runs were conducted with the same inflow parameters. The upstream area including the bulge was imaged in the first experiment and the adjacent downstream area was imaged in the second. The processed velocity and buoyancy fields from these two experiments are spliced together using a 3 cm overlapping region at  $x = 30$  cm. The field of view was 57 cm and 31 cm in the along- and across-shore directions, respectively. The two full-field runs are labelled FF1 and FF2 and are summarized in table 1 in the Appendix. In the second set of experiments, velocity and buoyancy in the bulge region of the plume were measured in a horizontal  $31 \times 31$  cm<sup>2</sup> section, 0.5 cm below the surface. The camera fields of view for this set of experiments and the last two sets of experiments are shown in figure 1. The horizontal bulge runs are denoted HB and are summarized in table 1 in the Appendix. In the third set, the vertical extent of the bulge was measured by imaging the buoyancy field in a vertical plane perpendicular to the coastal wall. The alongshore location of the plane was chosen so that it intersected the centre of the bulge circulation. The vertical bulge runs are denoted VB and summarized in table 2 in the Appendix. In the final set of experiments, the alongshore transport of buoyant water in the coastal current was measured using the angled laser-sheet technique. This measurement was made in a  $13 \times 13$  cm<sup>2</sup> area along the wall, 54 cm downstream of the source. These runs are labelled CC and are summarized in table 3.

## 2. Results

### 2.1. General plume description

In all of the runs described in this study, the inflowing buoyant water was observed to form a bulge near the source and a coastal current downstream of the bulge along the wall. The structure and evolution are shown in figure 2(a–c) for a typical plume. As described in the previous section, these figures were generated from two separate runs (FF1 and FF2), and the measured velocity and buoyancy fields were spliced together in the centre of the figure. The fields from the two runs blend seamlessly, implying that there was a high degree of repeatability from one run to the next.

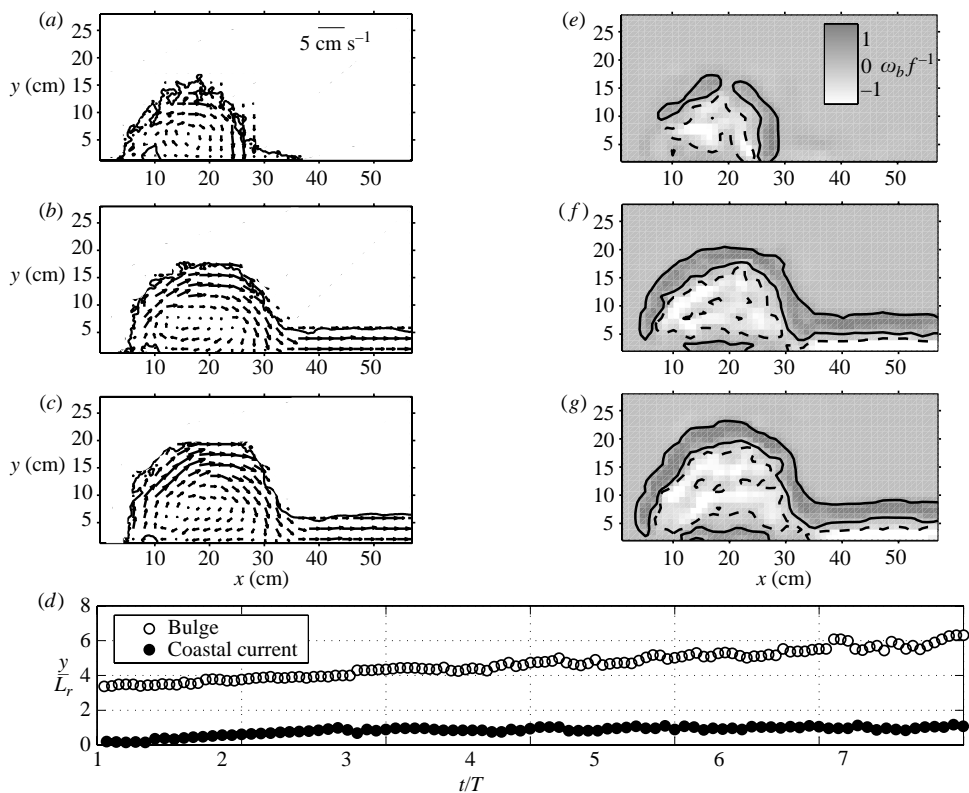


FIGURE 2. Temporal evolution of the plume. (a), (b) and (c), velocity fields after 1, 2 and 3 rotations periods, respectively. The outer contour marks 20% of the inflow buoyancy. (d)  $\circ$ , bulge and  $\bullet$ , coastal current widths normalized by the inflow Rossby radius,  $(g'H)^{1/2} f^{-1}$ , plotted against normalized time. (e), (f) and (g), plume vorticity normalized by the planetary vorticity,  $f$ , after 1, 2 and 3 rotations periods, respectively. The solid and dotted lines are the 0.4 and  $-0.4$  contours, respectively.

Once the source was turned on, buoyant water immediately separated from the wall and formed a broad jet-like current. The current was deflected to the right after half of a rotation period and impinged on the wall  $5L_r$  downstream of the source. After one period, the central vortex structure was established, and the coastal current began to form along the wall (figure 2a). After two and three rotation periods, the bulge widened further, but the coastal current width remained constant (figure 2b, c, d). The widths of the coastal current and bulge were measured based on the location of the maximum gradient in the buoyancy field and normalized by  $L_r$ . After the first three rotation periods, the coastal current width was slightly greater than  $L_r$ , and remained constant thereafter. The bulge continued to increase in size throughout the experiment, however, reaching approximately  $6L_r$  after seven rotation periods (figure 2d).

The anticyclonic circulation is also evident in the vorticity field generated from the measured velocity field (figure 2e, f, g). The centre of the bulge is dominated by a circular region of negative vorticity and bounded by a band of positive vorticity at its edge. As the bulge grows, the central anticyclonic region expands; however, the band



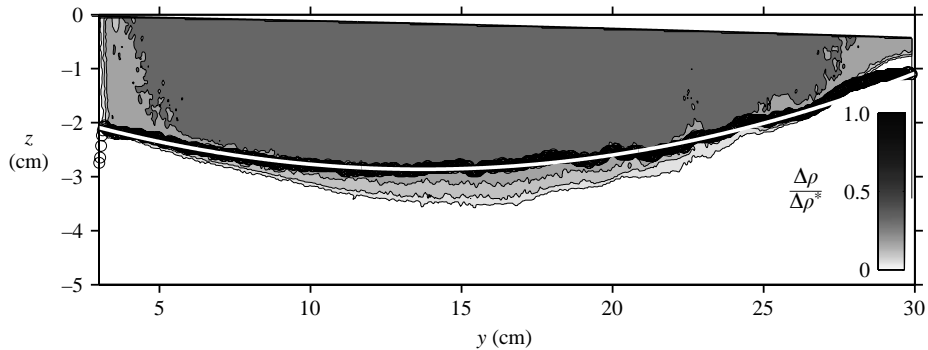


FIGURE 3. Vertical bulge section. Density anomaly in the vertical bulge section for Run VB6, normalized by the maximum density anomaly,  $\Delta\rho^*$ . The black circles mark the interface depth at each cross-shore point computed using the gradient method. The solid white line is a quadratic fit to the cross-shore depth profile.

of positive vorticity remains the same size. Equal amounts of positive and negative vorticity are introduced into the plume from the inflow, and, while the vast majority of the positive vorticity is carried downstream into the coastal current, most of the negative vorticity accumulates in the centre of the bulge. Despite the uniformity of the anticyclonic circulation in the core of the bulge, small frontal eddies are observed along the outer edge of the bulge, similar to those observed in coastal current flow by Griffiths & Hopfinger (1983). These are likely to enhance lateral exchange of momentum between the bulge and the ambient fluid in this region.

## 2.2. Bulge depth

In addition to its horizontal growth, the bulge adjusts vertically according to the density anomaly, rotation rate and inflow discharge. In the experiments described in table 2 (see the Appendix),  $Q$ ,  $f$  and  $g'$  are varied in order to examine the vertical and cross-shore variability of the bulge and to determine its depth.

The vertical buoyancy field in the bulge exhibits a predominantly two-layer structure (figure 3). The plume depth, defined at each point as the depth of the maximum vertical density gradient, varies quadratically in the cross-shore direction in the core of the bulge. Near the edge of the bulge there is more variability in the bulge structure, consistent with lateral mixing along the outer front of the plume. In this region, the gradient method over-estimates the depth. In order to calculate the depth profile, we fit a quadratic curve  $h = a_{h1}y^2 + a_{h2}y + a_{h3}$  to the locus of points corresponding to the bulge depth at each cross-shore location,  $y$  (figure 3). We use only points in the core of the bulge for the fit so that the fit is not affected by errors in the depth estimation near the bulge edge. The quadratic fit is successful in describing the bulge depth in every case.

The maximum bulge depth,  $h_b$ , based on the quadratic fit is plotted in figure 4(a) and normalized by the geostrophic scale,  $h_g$  in figure 4(b). This scale explains the variation in bulge depth for each of the independent variables,  $f$ ,  $g'$  and  $Q$ . The depth increases slightly over the course of the experiments. Other studies have reported exponential deepening of the bulge where  $h \sim t^n$ . For the present data, the exponent,  $n$ , is found to be less than 0.16. This result agrees well with the findings of Avicola & Huq (2003a); in their experiments, the normalized bulge depth increased from approximately 2 to 3 at a rate of  $\sim t^{1/5}$ . The slightly higher rate of deepening in their experiments relative to the present experiments was probably due to the

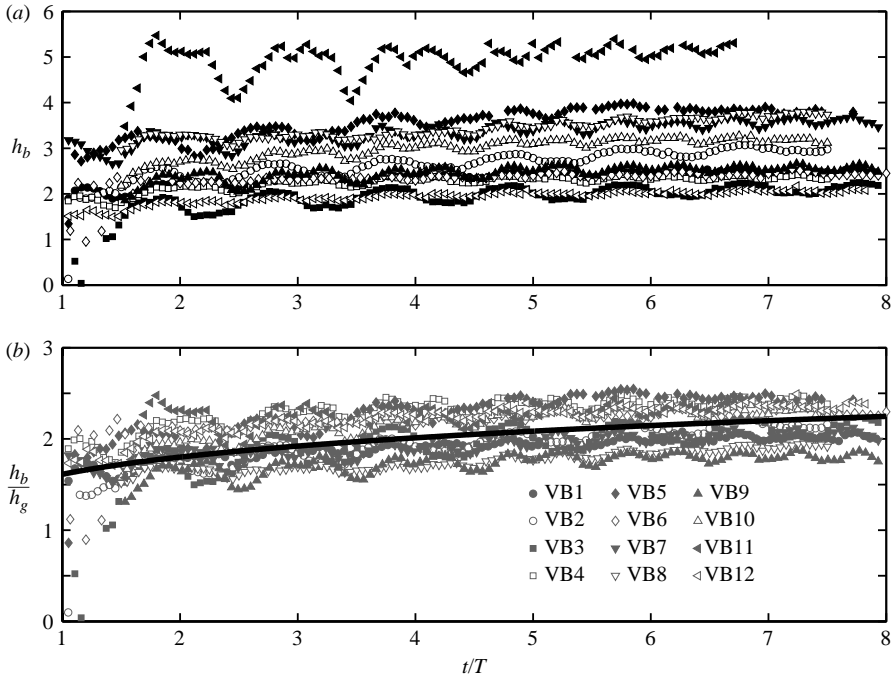


FIGURE 4. Bulge depth. (a) Maximum bulge depth based on a quadratic fit to the measured interface location. (b) Maximum bulge depth normalized by the geostrophic depth scale,  $h_g = (2Qf/g')^{1/2}$ . The solid black line is the exponential fit  $h_b/h_g = 1.6(t/T)^{0.16}$ .

difference in measurement techniques. If we define the bulge depth in terms of a reference buoyancy (20% of the inflow buoyancy) instead of the maximum vertical gradient, we observe greater deepening. This implies that the deepening may be due to mixing and dilution and may not represent a greater volume of buoyant fluid. In this analysis, the 20% contour is chosen as the reference buoyancy since isolines corresponding to lower buoyancy levels reflected more variability in the buoyancy field and were therefore more difficult to fit.

### 2.3. Offshore migration of the bulge centre

The velocity structure in the bulge is examined by considering the cross-shore profile of alongshore velocity in the bulge. The location of the profile is chosen so that it passes exactly through the bulge centre and thus represents the radial velocity distribution as closely as possible. A representative profile is plotted in figure 5. The velocity variation is strikingly linear in the core of the bulge. This is observed in the vast majority of runs and corresponds to the region of constant anticyclonic vorticity described in §2.1. Outside of the core region, on the inshore and offshore sides of the bulge, the velocity decreased rapidly to zero.

The offshore location of the bulge centre,  $y_c$ , is defined as the zero-crossing in the velocity profile. In practice,  $y_c$  was calculated using a linear fit to the velocities in the core of the bulge (dashed line in figure 5).

For all of the inflow parameters considered in this study,  $y_c$  increases linearly in time (figure 6). The variance in  $y_c$  is minimized when it is normalized by the inertial radius based on the mean inflow velocity,  $L_i = U/f$  ( $r^2 = 0.8$ ,  $p < 0.01$ ). Other scales

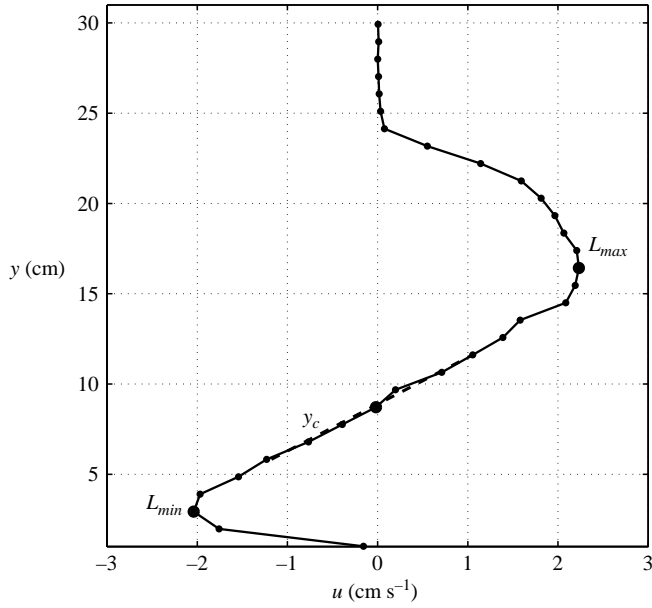


FIGURE 5. Cross-shore profile of alongshore velocity in the bulge. Small circles indicate data points and large circles indicate the bulge centre  $y_c$ , and the locations of the maximum and minimum velocities,  $L_{max}$  and  $L_{min}$ , respectively. The dashed line is a linear fit to the velocity in the core of the bulge.

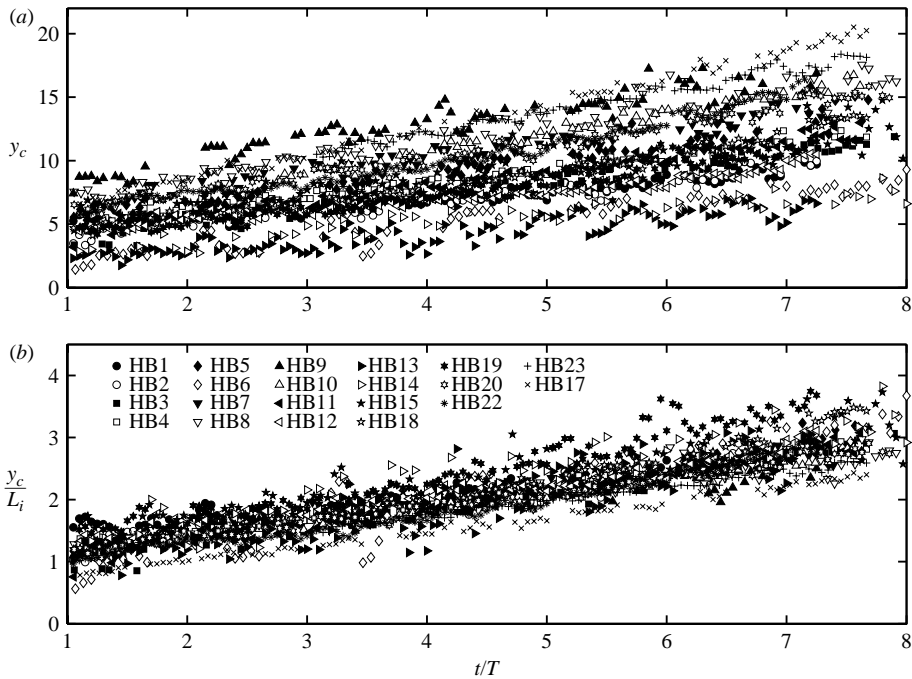


FIGURE 6. Bulge centre. (a) The offshore location of the center of the bulge,  $y_c$  according to the definition in figure 6. (b)  $y_c$  normalized by the inertial radius, for all runs.  $r^2 = 0.82$ ,  $p < 10^{-14}$ .

for bulge radius have been proposed and, although they do collapse the data, none explain as much of the variance (inflow Rossby radius,  $L_r$ ,  $r^2 = 0.57$ ,  $p < 0.01$ ; bulge Rossby radius,  $L_b$ ,  $r^2 = 0.66$ ,  $p < 0.01$ ; cyclostrophic radius,  $L_{cyc}$ ,  $r^2 = 0.61$ ,  $p < 0.01$ ). In particular, these alternative scales do not explain the bulge growth rate for runs with different inflow discharge rates,  $Q$ .

Based on the scaled location of the bulge centre, its evolution can be modelled by a simple linear expression,

$$\frac{y_c}{U/f} = \frac{C_y}{4\pi}tf + C_{y0}. \quad (2.1)$$

Here,  $C_y = 0.26 \pm 0.01$  is the dimensionless growth rate of the bulge and  $C_{y0} = 0.90 \pm 0.03$  is the initial bulge size. In dimensional terms,  $y_c$  is approximately equal to the inertial radius initially and moves offshore at a rate that is a function only of  $U$ .

A similar treatment of the alongshore dimension of the bulge indicates that, after an initial 2–3 rotation period adjustment, the alongshore migration of the bulge centre ceases or slows markedly. The alongshore dimension scales with the local Rossby radius, however, as opposed to the inertial scale. It appears, therefore, that the bulge expands preferentially offshore and that the cross-shore scale is not wholly representative of the bulge circulation.

The offshore location of the maximum and minimum velocities,  $L_{max}$  and  $L_{min}$ , are the outer and inner edges of the bulge core (figure 5). Based on these dimensions, the outer and inner radii are defined as  $r_o = L_{max} - y_c$  and  $r_i = y_c - L_{min}$ , respectively. Both radii scale with the inertial radius and both increase linearly over the course of each experiment; however,  $r_o$  is consistently larger than  $r_i$  (not shown). The slopes of the normalized  $r_o$  and  $r_i$  data are within 5% of each other, but the intercepts differ by approximately 1. In dimensional terms, the outer radius is consistently greater than the inner radius by one inertial radius. The bulge, therefore, is not exactly circular, but is clipped on the coast side, consistent with the conceptual models described in Nof (1988) and Fong & Geyer (2002).

#### 2.4. Bulge area

A direct measurement of the bulge area,  $A_b$ , is obtained by calculating the area included within the frontal buoyancy contour. As with the bulge depth, the plume edge is defined by the 20% buoyancy contour. For a number of runs, the bulge area is greater than the field of view and so the calculated area underestimates the true value. In order to account for this, the half-area for the left-hand half of the bulge is calculated based on the alongshore location of the bulge centre from §2.3. The total area is therefore estimated as twice the measured half-area. In each experiment, the area increases uniformly in time (figure 7a). In two cases, the growth rate appears to vary with the rotation period owing to variations in the uniformity of the illumination resulting from small errors in the laser alignment.

We define the effective bulge radius  $r_b$  representative of the bulge area as

$$r_b = \left( \frac{A_b}{\pi} \right)^{1/2}, \quad (2.2)$$

which is plotted in figure 7(b). As with  $y_c$ ,  $r_b$  was normalized by a number of possible scales and the results were compared. Whereas  $y_c$  scales with  $L_i$ , the variance in  $r_b$  is minimized when  $r_b$  is normalized by  $L_b$ , the bulge Rossby radius defined in (1.2d) (figure 7b). The total area of the bulge, therefore, depends on  $g'$  and the buoyant adjustment, as well as the rotation dynamics. Normalization of the bulge radius by

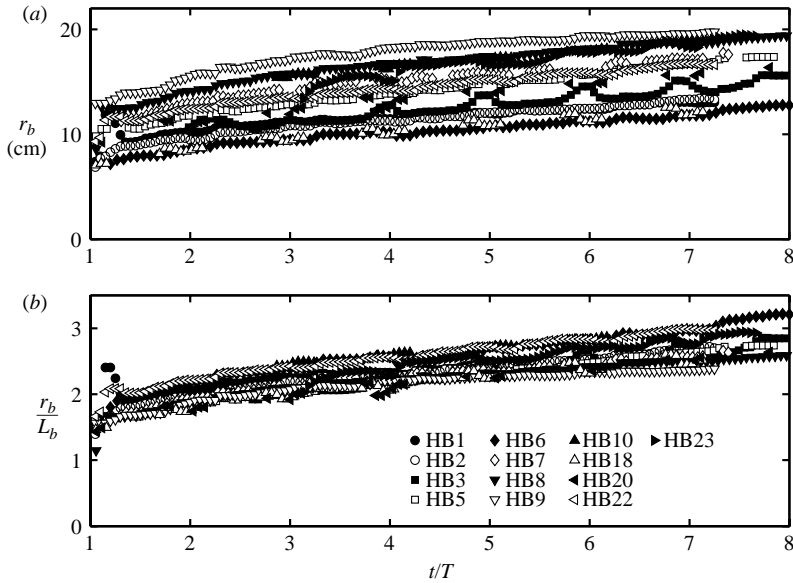


FIGURE 7. Effective bulge radius. (a) The effective bulge radius  $r_b$ , computed according to (2.2). (b) The effective radius normalized by the local Rossby radius,  $L_b$ . The radius increases as  $t^{0.25}$  initially and as  $t^{0.39}$  after the first 4 rotation periods.

$L_b$  is consistent with the analytical model of Nof & Pichevin (2001) and laboratory experiments performed by Avicola & Huq (2003a). The bulge grows as  $t^{0.25}$  during the first 5 rotation periods and as  $t^{0.39}$  at later times.

As described in §1.2, previous studies characterized the bulge by a single length scale. However, there is no consensus among the studies as to whether the inertial or Rossby radius is the relevant scale. The present results demonstrate that both are important; the inertial scale sets the offshore location of the bulge,  $y_c$ , and the Rossby radius sets the effective radius of the bulge,  $r_b$ . The bulge adjusts geostrophically such that its size is proportional to  $L_b$ . However, the inflow momentum determines its offshore expansion such that  $y_c$  is proportional to  $L_i$ .

### 2.5. Plume momentum balance

Next, the momentum balance in the bulge and coastal current are estimated. The proposed bulge momentum balance, given by (1.1), is evaluated using the averaged cross-shore profiles of alongshore velocity described in §2.3 and cross-shore depth profiles computed in §2.2. The two terms on the left-hand side of (1.1), the centrifugal and Coriolis accelerations, are calculated from the velocity profiles. The pressure term on the right-hand side is calculated using the slope of the lower interface from the quadratic fit to the depth profile. In order to evaluate the momentum balance, the cross-shore variations in  $u$  and  $h$  in the slice through the bulge centre are assumed to be equivalent to radial variations. Based on (2.1), the momentum contribution due to the offshore migration of the bulge for the experiments considered here is  $O(0.02 \text{ m s}^{-2})$ , at least an order of magnitude smaller than the dominant terms in the momentum balance.

The three dominant terms in the momentum balance are plotted with respect to the distance from the wall in figures 8(a), 8(b) and 8(c) for runs with  $Fr = 0.57$ , 0.81 and 1.00, respectively. No consistent trend is observed in the magnitude of the

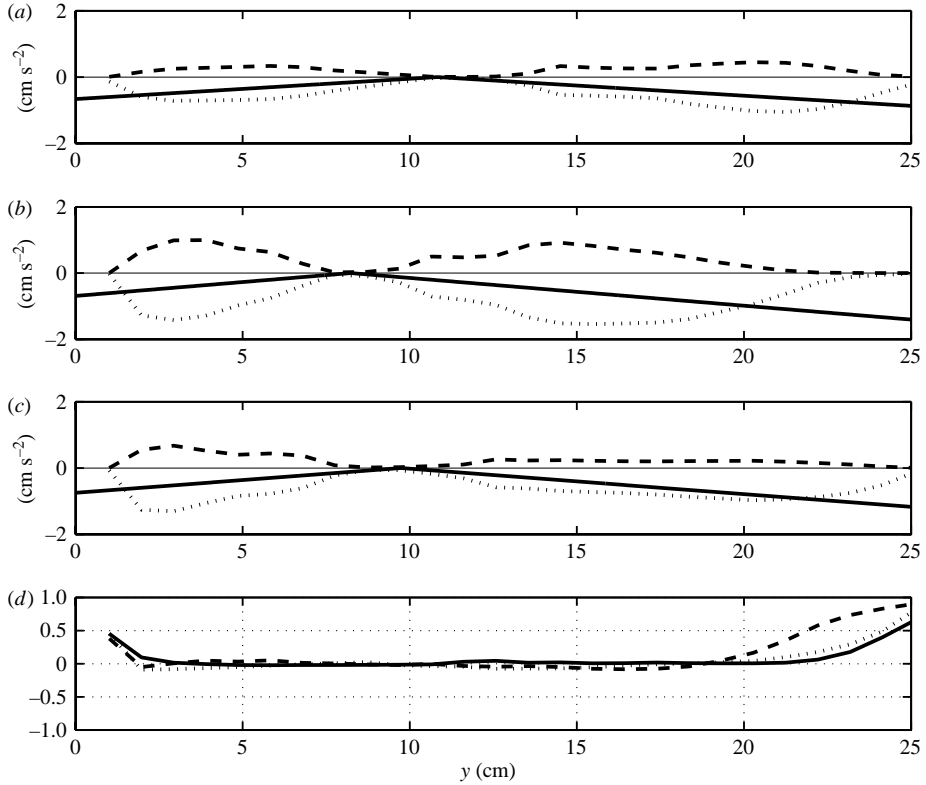


FIGURE 8. Bulge momentum balance. The terms in a gradient–wind momentum balance,  $v_\theta^2/r$ ,  $fv_\theta$  and  $g'(\partial h/\partial r)$ , are plotted in (a)–(c) for three different cases after approximately 6 rotation periods. —,  $g'(\partial h/\partial r)$ ; ---,  $u^2/r$ ; ···,  $uf$  (a)  $Fr = 0.57$  and  $Ro = 0.84$ , (b)  $Fr = 0.81$  and  $Ro = 0.67$  and (c)  $Fr = 1.00$  and  $Ro = 0.62$ . In (d) the normalized residual of the momentum balance is plotted; —,  $Fr = 0.57$ ; ---, 0.81; ···, 1.00.

momentum terms with  $Fr$ . However, the ratio of the centrifugal to the Coriolis term remains relatively unchanged over the parameter space investigated. The normalized momentum residual, defined as  $(v_\theta^2/r + fv_\theta - g'(\partial h/\partial r))/\max(fv_\theta)$ , is less than 10% in the core of the bulge, indicating that the dynamics in this region are described well by the gradient–wind balance in all three cases considered (figure 8d). The balance breaks down toward the edges of the bulge, where momentum is probably lost because of frictional effects. These include lateral exchange of momentum due to small frontal eddies and viscous diffusion in the thin outer region of the bulge.

Although the offshore migration of the bulge is a very small contribution to the momentum balance within the bulge, it is likely to be important to the integrated momentum of the entire plume circulation. Nof & Pichevin (2001) hypothesize that the integrated momentum due to the offshore migration of the bulge is necessary to balance the flux of momentum into the coastal current.

The alongshore momentum in the coastal current is expected to be in geostrophic balance (e.g. Garvine 1995). This is evaluated using the angled-slice technique, which allows direct measurement of the velocity and density fields (figure 9a, b).

The geostrophic velocity is computed from the measured density field using

$$u_g = -\frac{g}{f} \frac{\partial}{\partial y} \int_{-z}^0 \frac{\Delta\rho}{\rho_o} dz. \quad (2.3)$$

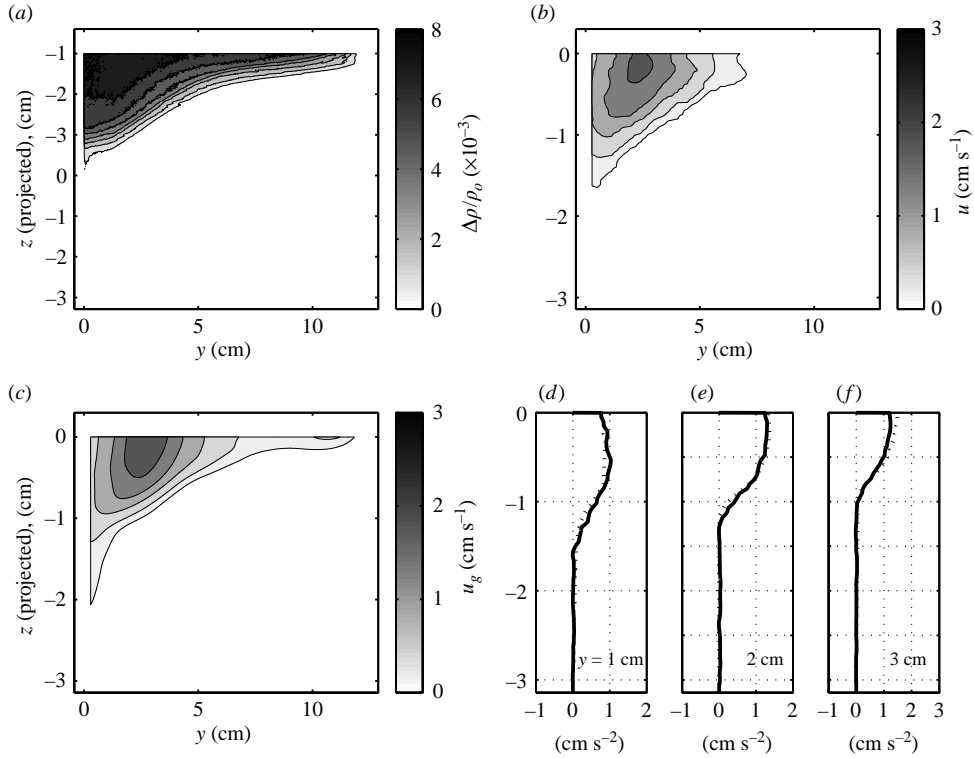


FIGURE 9. Coastal current structure. (a) The measured density anomaly,  $\Delta\rho/\rho_o$  in a  $y-z$  slice through the coastal current. Since the data were acquired using the angled-slice technique, the  $z$ -coordinate is projected from the angled plane into a vertical plane. (b) Measured along-shore velocity in the coastal current. The spatial resolution is approximately 0.1 and 2 mm for the density and velocity measurements, respectively. (c) Geostrophic velocity computed using (2.3) and the measured density anomaly from (a). (d), (e) and (f), comparison of the cross-shore pressure gradient term with the Coriolis term in the geostrophic momentum balance for vertical sections 1, 2 and 3 cm from the wall, respectively.

The structure of the measured alongshore velocity field closely matches the computed geostrophic velocity (figure 9c). In the core of the current, the velocity magnitude is typically within 10% of  $u_g$ . The departure from geostrophy is greatest at the offshore edge of the coastal current owing to the lateral spreading of the surface layer, and close to the surface and interface where viscous diffusion becomes important. The cross-shore pressure gradient,  $-(1/\rho_o)(\partial p/\partial y)$ , and the Coriolis term,  $fu$ , are compared in figures 9(d), 9(e) and 9(f) for vertical profiles located 1, 2 and 3 cm from the wall, respectively. These profiles clearly demonstrate that the momentum balance in the core of the coastal current is geostrophic.

### 2.6. Coastal current transport

The alongshore transport of buoyant water in the coastal current is calculated directly from the measured velocity and buoyancy fields according to,

$$Q_{fw} = \int \int \frac{\Delta\rho}{\rho_o} u(y, z) dz dy. \quad (2.4)$$

Equation (2.4) is integrated over each image excluding the region above the water surface and beyond the wall. The data is filtered using a low-pass Butterworth filter with a width equal to the rotation frequency. The measurement location is 54 cm

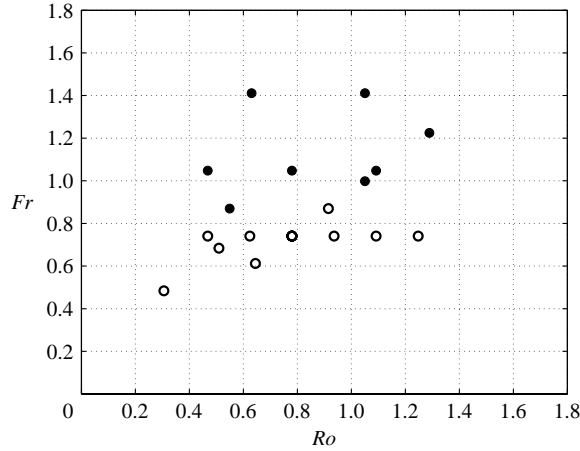


FIGURE 10. Stability diagram for all CC runs.  $\circ$ , Stable and  $\bullet$ , unstable runs are marked with open and solid circles, respectively.

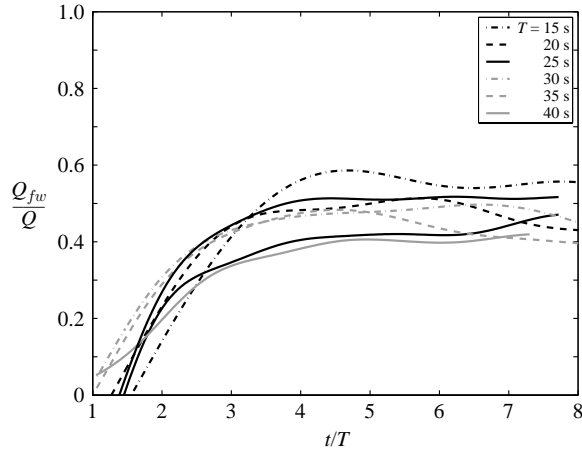


FIGURE 11. Time series of filtered normalized alongshore transport for different rotation rates.

downstream of the source and, therefore, the transport at that location is subject to a time lag associated with the advective travel time of the coastal current.

There are three modes of coastal current transport: slowly increasing, oscillatory and steady. In the slowly increasing mode, which is observed only in runs with low inflow discharge, the transport increases for the entire duration of the experiment. In these runs, the coastal current thickness is of the order of the Ekman-layer thickness and frictional effects are probably important. Since this is not relevant to naturally occurring plumes, these runs are not discussed further. The oscillatory mode corresponds to instability upstream in the bulge that modifies the flow into the coastal current. This is verified and discussed further in §2.7. The plume displays this unstable behaviour for all runs with  $Fr_i > 0.9$  (figure 10).

In the steady mode, the transport increases during the first 3–4 rotation periods and is constant thereafter (figure 11). The peak velocity in the coastal current is observed only 0.5 rotation periods after the current arrives at the measurement location. After



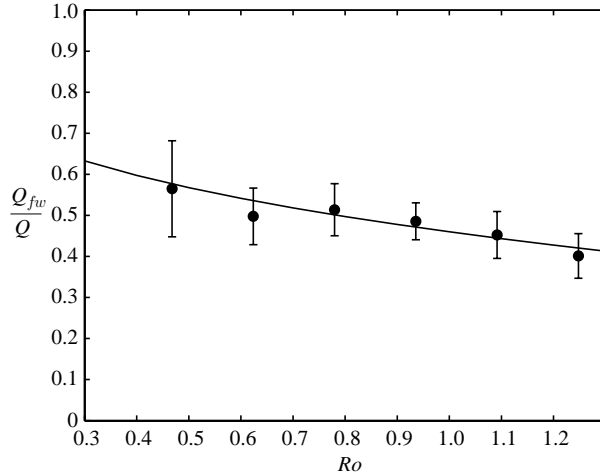


FIGURE 12. Normalized mean coastal current transport for runs in which only the table rotation rate was varied (CC1–CC4, CC6 and CC11). Error bars show the standard deviation which is approximately 0.07 for each experiment. The line is an exponential curve fit,  $Q_{fw}/Q = 1 - 0.54Ro^{0.32}$ .

that time, the current velocity decays, as was observed in Lentz & Helfrich (2002). The current width and depth both increase during the ramp-up period and are relatively constant for all subsequent time.

Once the coastal current has achieved steady state, it transports between 40 and 60 % of the source discharge in the parameter range considered. The average steady transport for each run, calculated using data after 4 rotation periods, depends on the rotation rate (figure 12). The normalized transport decreases from 0.56 to 0.41 between Rossby numbers of 0.47 and 1.25. The curve shown in figure 12 is a least-squares fit to the data given by  $Q_{fw}/Q = 1 - aRo^b$ , where  $a = 0.54 \pm 0.04$  and  $b = 0.32 \pm 0.18$ . The functional form of this fit is discussed in depth in §3, where it is shown that the observed decrease in transport with  $Ro$  is consistent with other laboratory studies, numerical modelling studies and the observed bulge growth rates.

### 2.7. Bulge oscillation

Most runs with high inflow discharge or low density anomaly became unstable after 5–6 rotation periods. The velocity and density fields for one such run (Run HB19,  $Ro = 0.62$ ,  $Fr = 1.00$ ) are shown in figure 13. As the bulge becomes unstable, the location where the outer bulge current impinges on the wall moves upstream, cutting off flow into the coastal current and increasing flow into the bulge. At this time, the bulge moves offshore more quickly and eventually pinches off. No runs showing the bulge region were carried out for long enough to observe the bulge circulation being reset after pinch-off. We expect that the increased retention of flow in the bulge will eventually cause it to expand and reattach to the wall and coastal current. This is verified using numerical model results (described below) and is evident in measurements of coastal current transport.

A vertical bulge section for run VB11 after approximately 7 rotation periods is shown in figure 13(d). This run is also unstable and the separation from the wall is evident. While a small amount of buoyant fluid remains against the wall to drive an alongshore flow, most of the bulge has migrated away.

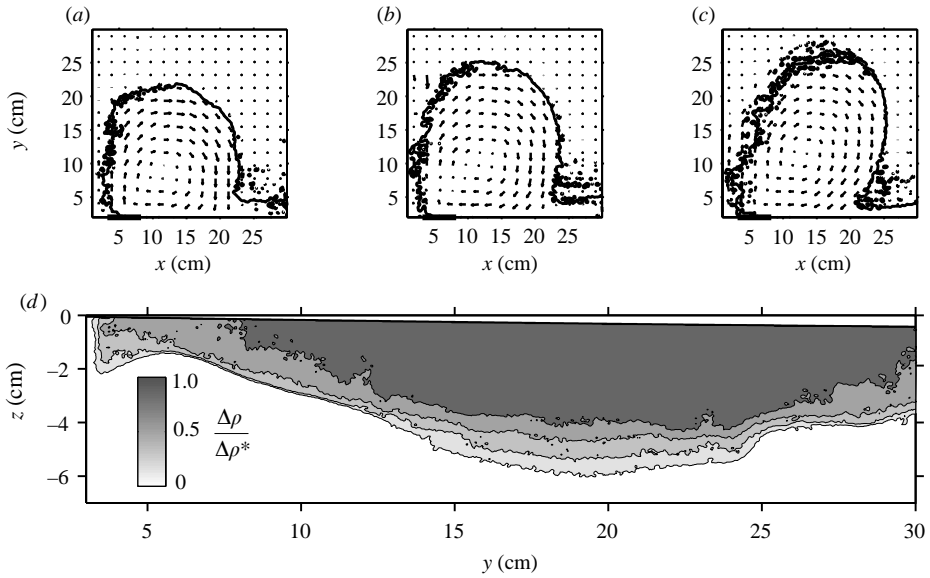


FIGURE 13. Bulge pinch-off. (a), (b) and (c) Velocity and density fields for run HB19 after 5, 6 and 7 rotation periods, respectively. (d) Vertical section through the bulge for run VB11. Runs HB19 and VB11 do not have identical inflow parameters; however, both are good examples of bulge pinch-off. Note that the clipped appearance of the density field on the left-hand side of the bulge in (a)–(c) is due to attenuation of the laser and does not reflect the actual shape of the bulge.

For comparison, a relatively high  $Fr$  ( $=1.0$ ) run was also conducted using a numerical model similar that used by Fong & Geyer (2002). The model output clearly shows the same pinch-off phenomenon as the laboratory experiments (figure 14). In the numerical model run, the bulge reattaches after pinch-off and then grows again until pinch-off reoccurs and the pattern repeats itself. Similar oscillation and eddy shedding was also observed for high  $Fr$  runs in a set of preliminary dye experiments (not shown).

The observed oscillatory behaviour in the bulge affects the discharge of buoyant water into the coastal current. As the bulge moves away from the wall, it separates from the coastal current, increasing the return flow to the bulge and limiting the flow into the coastal current. The coastal current transport increases initially and then decreases as the bulge pinches off. This behaviour is observed in the coastal current for a number of runs, typically with either high  $Q$ , low  $g'$ , or both (figure 15).

As mentioned previously, it was not possible to observe the longer-time behaviour of the bulge in the laboratory experiments because it outgrew the camera field of view. This limitation did not apply to measurements in the coastal current, however. Three laboratory experiments were carried out for longer than 8 rotation periods. In these runs, the coastal current transport repeats the pinch-off cycle 2–3 times at intervals equal to approximately 9 rotation periods. The time between consecutive transport maxima is equal within each of these runs, indicating that the same mechanism is repeating itself. The period of oscillation in the coastal current is approximately the same in the numerical model runs (figure 14) as well as the preliminary dye experiments. The qualitative and quantitative agreement between the numerical and laboratory experiments indicates that the same mechanism is observed in both.

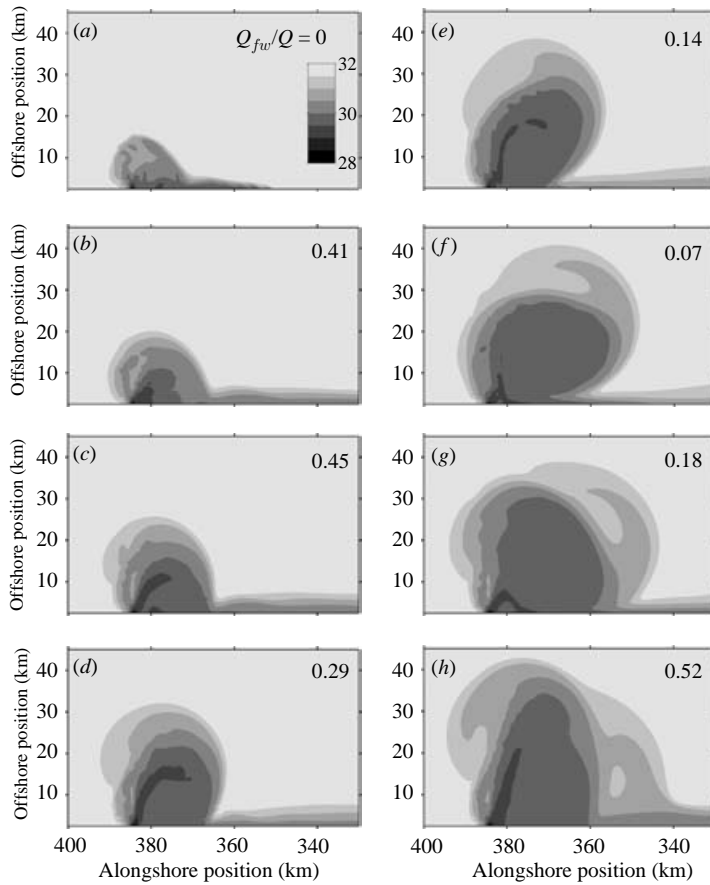


FIGURE 14. Salinity fields from a numerical model run with  $Fr = 1.0$ . The panels correspond to (a) 1, (b) 3, (c) 5, (d) 7, (e) 9, (f) 11, (g) 13 and (h) 15 days. The fraction of the inflow transported in the coastal current is given in each panel. The bulge is observed to alternately pinch-off and reattach to the wall causing the coastal current flow to be pulsed.

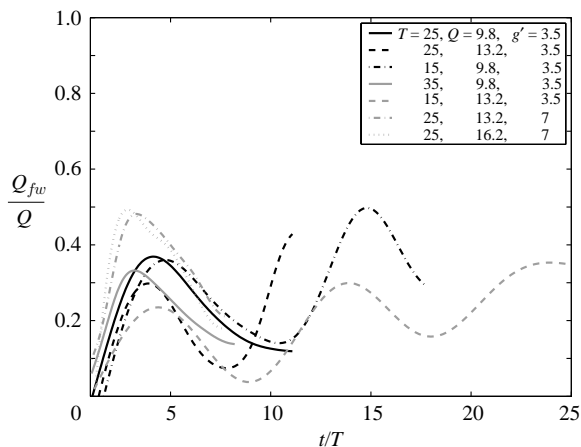


FIGURE 15. Time series of filtered alongshore transport for all unstable runs.

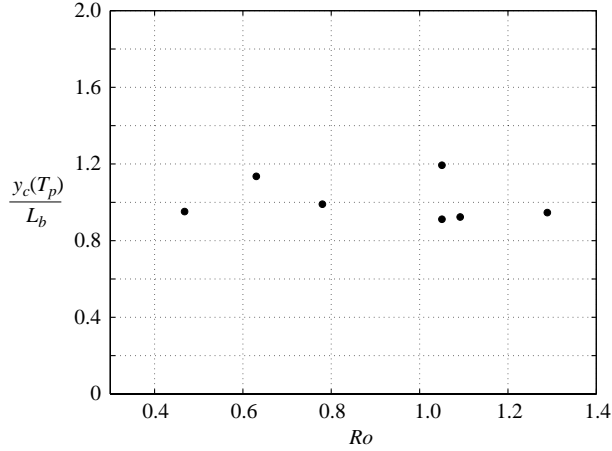


FIGURE 16. Location of the bulge centre normalized by the local Rossby radius at the instability time.

We hypothesized above that, in the process of pinching off, the bulge fluid is advected downstream in the coastal current. We would thus expect to see periodic bursts in the coastal current exceeding  $Q$ . Instead, we observe that the transport increases to a higher value each cycle; however, it does not exceed  $0.6Q$  in the course of any of the runs. This implies that only a fraction of the bulge sloughs off into the coastal current during the pinch-off. While the pinch-off and re-attachment sequence appears oscillatory in character, the magnitude of the oscillation increases throughout the run in both the laboratory and numerical model experiments. Owing to this amplification, the observed oscillation is eventually expected to result in breakdown of the bulge circulation and is therefore considered to be a fundamental instability of the system.

In order to examine the character of the instability in greater detail, we define the pinch-off time,  $T_p$ , corresponding to the first maxima in the coastal current transport. The offshore location of the bulge centre at the pinch-off time,  $y_c(T_p)$ , is calculated from (2.1). In figure 16,  $y_c(T_p)$ , normalized by the bulge Rossby radius, is plotted for all unstable coastal current runs. The bulge becomes unstable when  $y_c(T_p) = bL_b$ , where  $b = 1.0$  is a constant, based on the mean value of the data presented in figure 16. Normalizing this expression by  $L_i$  shows that the bulge location at the point of pinch-off depends inversely on the ratio of scales,  $L_*$ , i.e.

$$\frac{y_c(T_p)}{L_i} = \frac{1}{L_*}. \tag{2.5}$$

Furthermore, since the bulge radius  $r_b$  scales with  $L_b$ , this result implies that the bulge becomes unstable when its centre moves offshore a fixed distance relative to its radius. By combining the above result with the results for  $r_b$ , the bulge is found to become unstable when

$$\frac{y_c}{r_b} = 0.69 \pm 0.07.$$

A circular bulge will detach when  $y_c/r_b$  is unity because the distance from the bulge centre to the wall is greater than its radius. In that case, the recirculating bulge current is tangent to the wall and the effective incidence angle is  $180^\circ$ . It is not

surprising, therefore, that the instability is initiated when  $y_c/r_b < 1$ . Whitehead (1985) showed that the angle formed between an impinging jet and a wall in a rotating system determines the flux of fluid in either direction along the wall. According to his theory, the flux of fluid downstream (into the coastal current) is reduced as the angle of the impinging current is increased. As the bulge moves offshore, and  $y_c$  approaches  $r_b$ , the angle that the bulge current makes with the wall increases beyond  $90^\circ$ . It is likely, therefore, that the flow into the coastal current is significantly reduced prior to the time of detachment and pinch-off is initiated. This is consistent with observations of the bulge structure, such as those in figures 13 and 14(c)–14(e), which indicate that the coastal current transport is reduced before the bulge detaches.

### 3. Discussion

In the present experiments, the plume is observed to evolve as follows. Inflowing buoyant water separates immediately from the wall and forms a jet that circumscribes the bulge. The jet impinges on the wall downstream of the bulge where it is divided into a flow that forms the coastal current and one that rejoins the bulge circulation, as was proposed by Whitehead & Miller (1979). The latter flow is incorporated into a region of uniform anticyclonic vorticity in the centre of the bulge, which accumulates buoyant water, in most cases at a constant rate, and expands.

The cross-shore momentum balance in the coastal current downstream of the bulge is confirmed to be geostrophic. The circulation in the bulge deviates significantly from the geostrophic balance that is often assumed in river plumes owing to the importance of the centrifugal acceleration. The bulge momentum is found to be in gradient–wind balance, as was hypothesized by Yankovsky & Chapman (1997), and friction does not play a primary role in plume dynamics in the bulge (figure 8). This is not surprising since the Ekman-layer depth is of the order of 1 mm, less than 10% of the typical bulge depth. Viscous diffusion and lateral mixing are likely to be more important near the edge of the bulge, however, where the plume is thin.

In similar laboratory experiments, Avicola & Huq (2003a) found that the bulge depth and radius scaled with a geostrophic depth scale,  $h_g$ , and the Rossby deformation radius based on that depth,  $L_b$ , respectively. They found that the depth and radius increased as  $t^{1/5}$  and  $t^{2/5}$ , respectively. The results of the present experiments confirm their proposed scaling. The depth and radius increase as  $t^{0.16}$  and  $t^{0.39}$ , respectively. The small difference between observed growth rates can be attributed to different measurement techniques, as described in §2.2, and is within the error of both sets of measurements. This scaling suggests that the dominant dynamical balance in the bulge circulation is geostrophic. However, it was shown in §2.5 that the bulge is in gradient–wind balance and that the nonlinear terms are of the same order as the Coriolis and pressure gradient terms. In the present experiments, a second scale,  $y_c$ , is also found to be significant in the evolution of the bulge.  $y_c$  is the offshore location of the centre of the anticyclonic circulation in the bulge. It is observed to be proportional to the inertial radius  $L_i$ . Since  $L_i$  depends on the inflow velocity, the importance of this scale to the evolution of the bulge suggests that inflow momentum determines the cross-shore expansion of the bulge.

There are two length scales, therefore, that determine the bulge dynamics,  $r_b \sim L_b$  and  $y_c \sim L_i$ . The ratio of  $y_c$  to  $r_b$ , describes the location of the bulge centre relative to its mean radius. When  $y_c/r_b$  is relatively small, the bulge is held close to the wall relative to its radius. When  $y_c/r_b$  is larger, but less than 0.7, the bulge circulation

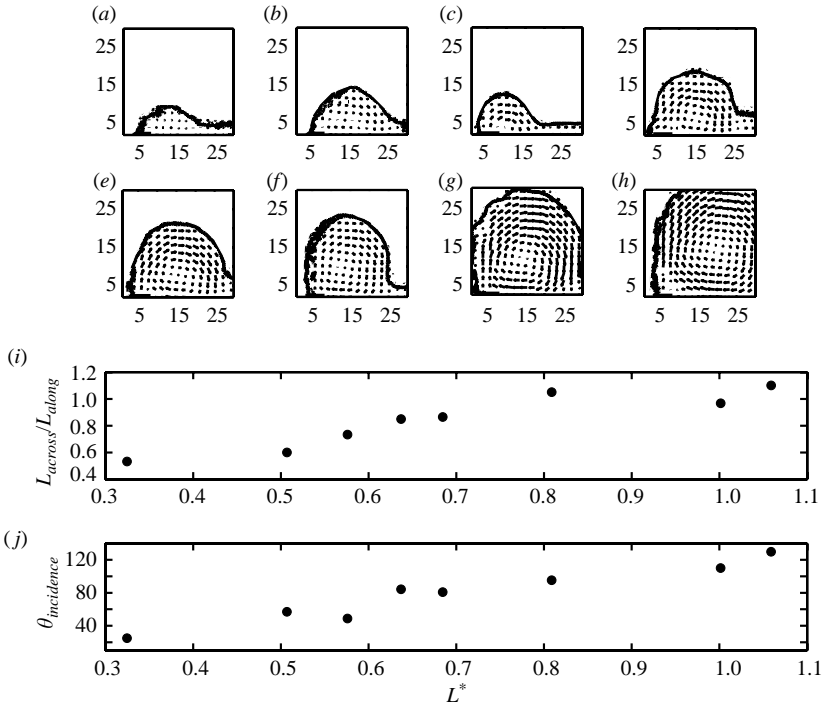


FIGURE 17. Qualitative change in bulge shape with increasing  $L^*$ . The velocity (arrows) and density (contour line) fields are shown for 8 different runs after 5 rotation periods.  $L^*$  is (a) 0.32, (b) 0.51, (c) 0.58, (d) 0.64, (e) 0.68, (f) 0.81, (g) 1.0 and (h) 1.1, respectively. As  $L^*$  increases, the bulge moves offshore, becomes more circular and the ratio of the bulge width to the coastal current width increases. In (i), the ratio of the cross-shore width to the alongshore width is plotted for each run. In (j), the incidence angle of the bulge current is plotted for each run. The scale ratio and angle for the highest  $L^*$  is an approximation since the edges of the bulge have passed out of the field of view.

is not held as closely to the wall. When  $y_c/r_b \geq 0.7$ , the bulge circulation is forced offshore relative to its radius. In this case, the bulge fills more rapidly, becomes unstable and pinches off.

Nof (1988) and Fong (1998) both developed related conceptual models. They described the bulge as a circle that is clipped by the wall and suggested that the discharge of buoyant fluid from the bulge is related to the clipped area. The model described above extends their work by presenting separate scales that determine the size and location of the bulge, thereby providing a means of estimating the clipped area. Although we do not calculate the clipped area, we show in the following analysis that the discharge into the coastal current is consistent with this geometric model.

The bulge structure is expected to vary with  $L^* = L_i/L_b$  based on the above conceptual model. In figure 17, the velocity and density fields after 5 rotation periods are shown for 8 runs spanning a range from  $L^*$  equal to 0.32 to 1.1. The shape of the bulge changes considerably over this range, with the bulge circulation moving offshore as  $L^*$  increases. This can be quantified based on the bulge asymmetry  $L_{cross}/L_{along}$ , which is the ratio of the cross-shore to the alongshore width of the bulge. Low  $L^*$  runs have low values of this asymmetry parameter and are held close to the wall

(figure 17*i*), whereas the asymmetry parameter exceeds unity for large  $L^*$  runs, which extend away from the wall. Because of this asymmetry, the angle that the impinging bulge current makes with the wall at the stagnation point increases as the centre of the bulge moves away from the wall (figure 17*j*). As shown by Whitehead (1985), this decreases the discharge of buoyant fluid from the bulge into the coastal current. The observed decrease in the ratio of the coastal current width to the bulge width with increased  $L^*$  is consistent with this prediction (figure 17*a–h*).

In the preceding analysis, the time dependence of  $r_b$  and  $y_c$  was ignored. Nevertheless, it plays an important role in the dynamics of the plume. In all of the experiments reported in this study,  $r_b$  was initially greater than  $y_c$ , and thus the bulge was initially stable. In cases where the plume became unstable,  $y_c$  increased until it was greater than  $0.7r_b$ . Since  $y_c$  was initially smaller than  $r_b$  and increased more rapidly, the bulge should eventually become unstable in all cases. This could not be tested in the present laboratory experiments because the size of the tank and field of view limited the duration of the runs. Numerical model runs carried out for much greater times (e.g. Nof & Pichevin 2001; Fong & Geyer 2002) and moderate  $Fr$ , however, do not result in this instability. We hypothesize that, after a certain time  $t_o$ , the recirculating flow in the bulge is much greater than the source discharge and, therefore, the momentum contribution from the source becomes less significant. At this point, it is likely that the bulge is not forced offshore as rapidly and may remain stable. Nof & Pichevin (2001) make a similar distinction between the plume initiation time ( $t < t_o$ ) and the long-time evolution of the plume, for which their analytical theory applies. The results presented here indicate that the plume initiation time, during which nonlinearity is very important, is at least 8 days. This time period is critical to naturally occurring river plumes, since the time scales of variation due to winds and other external forcing is of the order of 2–10 days (Hickey *et al.* 1998).

The results of these experiments provide additional verification of the conclusions of Avicola & Huq (2003*a*) and Whitehead & Miller (1979), who found that the bulge size scales with the Rossby deformation radius. In the present study, however, the inflow geometry is quite different from the geostrophic inflows used in the above studies. The direct non-geostrophic inflow must adjust rotationally as it enters the basin. This may contribute to the observed difference between cross- and along-shore bulge scales, which are proportional to the inertial and Rossby radii, respectively.

A primary objective of this work has been to quantify and explain the reduction in alongshore transport in the laboratory plume owing to formation of the anticyclonic bulge circulation. It is clear from the bulge experiments that the reduction is associated with the continual growth of the bulge and accumulation of fluid within it. Furthermore, the size of the bulge relative to its offshore location results in a geometric constraint that alters the discharge of buoyant fluid into the coastal current. When  $L^*$  is high, the bulge forms a more complete circle, is further from the wall, and discharges less fluid into the coastal current. The reduction in transport with increased  $L^*$  is supported by direct measurements of coastal current transport. Since  $L^* = 2^{-1/4} Ro^{1/4} Fr^{1/2}$  (see §1.3.1), the preceding geometric description of the bulge circulation suggests that coastal current transport will decrease for higher  $Fr$  and  $Ro$ . This  $Ro$  dependence was observed in the transport experiments (figure 12) and the numerical model data of Fong & Geyer (2002) (figure 18). The dependence on  $Fr$  was also evident in the transport experiments; however, the observed variability was more complex. Increased  $Fr$  decreased the transport considerably and resulted in

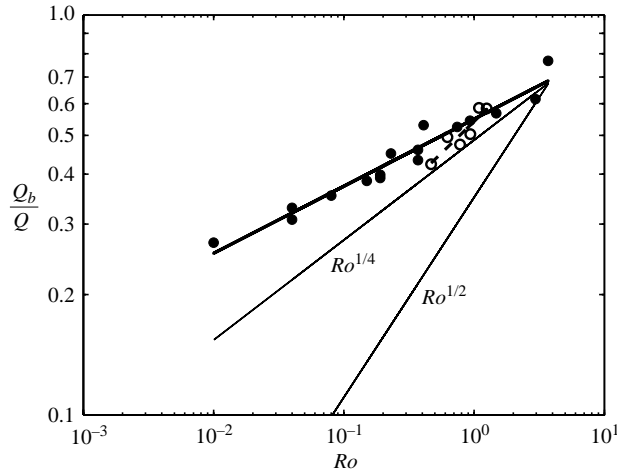


FIGURE 18. Normalized rate of accumulation in the bulge plotted versus inflow Rossby number including  $\circ$ , laboratory data from the present study and  $\bullet$ , numerical data from Fong & Geyer (2002). —, fit to numerical data; ---, fit to laboratory data.

unsustainable offshore bulge growth and eventual pinch-off. For further confirmation, the numerical model data of Fong & Geyer (2002) were re-plotted in terms of  $Fr$ , using inflow parameters listed in their tables 1 and 2. The trend in their data also supported the above conceptual model in which the transport is lower for higher  $Fr$  (not shown).

The dynamical dependence of the coastal current transport on inflow parameters can be elucidated by considering the conservation of volume in a rectangular control volume that includes the entire bulge and the beginning of the coastal current. Fluid enters the control volume from the river at rate  $Q$  and leaves in the coastal current at rate  $Q_{cc}$ . The difference  $Q_b = Q - Q_{cc}$ , is the rate of accumulation of fluid in the bulge owing to its expansion. If the bulge is assumed to be circular,

$$Q_b = 2\pi \frac{d}{dt} \int_0^R hr \, dr, \tag{3.1}$$

where  $R$  is the time-dependent radius of the bulge. As a first approximation and mathematical convenience, let  $h(r, t) = \bar{h}$ , where the dependence of  $h$  on  $r$  is assumed to be negligible such that

$$Q_b = \pi \frac{d}{dt} \bar{h} R^2 = Q - Q_{cc}. \tag{3.2}$$

For the purposes of scaling comparisons, (3.2) relates the bulge growth to the reduction in alongshore transport. In §§2.2 and 2.4, the bulge depth and radius were found to vary as  $t^{0.16}$  and  $t^{0.39}$ , respectively, after an initiation period. According to (3.2), the observed time dependence suggests that the coastal current transport will be constant, within the error of the experiments. During the initiation period, however, the bulge growth rate is slower, and more fluid must be discharged into the coastal



current. This may correspond to the ramp-up period observed in the coastal current transport experiments.

In the case of geostrophic flow in the bulge,  $\bar{h} \sim (2Qf/g')^{1/2}$  and  $R = r_b \sim (2g'Q/f^3)^{1/4}$ . Thus, the normalized bulge growth scales as

$$\frac{Q_b}{Q} = \frac{\pi}{Q} \frac{d}{dt} \bar{h} L_b^2. \quad (3.3)$$

In this case,  $Q_b/Q$  is constant and does not depend on  $t$ ,  $Ro$  or  $Fr$ .

If the bulge radius is assumed instead to scale with the inertial radius,

$$\frac{Q_b}{Q} = \frac{\pi}{Q} \frac{d}{dt} \bar{h} L_i^2 \sim Fr Ro^{1/2}. \quad (3.4)$$

In reality, however, it is clear that both the inertial and geostrophic scales are important in describing the bulge growth. Using the simplest combination of these two scales, if the bulge area scales according to  $R^2 \sim L_i L_b$ , then the bulge growth scaling is given by

$$\frac{Q_b}{Q} = \frac{\pi}{Q} \frac{d}{dt} \bar{h} (L_i L_b) \sim Fr^{1/2} Ro^{1/4}. \quad (3.5)$$

It should be noted that, according to the conceptual model of a clipped circle described above, the bulge area can be calculated exactly as a geometric function of the radius and distance to the wall. In choosing to scale the bulge area as  $L_i L_b$ , we have significantly simplified the actual dependence on the two scales; the exact scaling may be more complex and hence the Rossby-number dependence different from the 1/4 power law derived above. Nevertheless, the simple scaling illustrates how the inclusion of both scales leads to a Rossby- and Froude-number dependence, which is observed in the plume behaviour and the coastal current transport.

In the presents experiments, the coastal current was measured directly using the angled-slice technique. For runs with a stable bulge, the freshwater transport was observed to range from approximately 40 % to 60 % of the total freshwater discharge. This range is consistent with the experiments of Gleizon *et al.* (1996), who estimated that the transport in the majority of their runs ranged from 40 % to 70 %. The agreement with the latter study, which consists of an exchange-type inflow and an experimental apparatus that is seven times as large, implies that the present results are insensitive to the type of inflow used or the scale of the experiment. Avicola & Huq (2003a) estimate that the alongshore transport is approximately constant and between 35 % and 40 % of the inflow.

As mentioned previously, measurement of the coastal current transport was limited to runs in which the bulge was stable and only variation of the Rossby number could be determined systematically. In these experiments, the non-dimensional coastal current transport is lower for runs with lower table rotation rates. According to (3.2), this implies that  $Q_b$  must be higher for higher  $Ro$  runs.  $Q_b/Q$  is calculated using (3.2) and the transport data shown in figure 12 and plotted as a function of  $Ro$  in figure 18. Regression of the laboratory data alone results in bulge growth that scales as

$$\frac{Q_b}{Q} \sim Ro^{0.32 \pm 0.18}.$$

The observed dependence on the Rossby number confirms that the purely geostrophic scaling in (3.3) is not valid. The Rossby number exponent matches the exponent of 0.25 obtained using both inertial and geostrophic scales within the experimental error. Although the confidence intervals are relatively large on this measurement owing to the limited parameter range available, the observed exponent is statistically different from 0 and 0.5 and supports the proposed scaling.

For comparison, values of  $Q_b/Q$  derived from Fong & Geyer's (2002) numerical model data are also plotted in figure 18. In their study, they modelled the flow of buoyant water from a simple discharge source into a flat-bottom rectangular basin using ECOM3D, a derivative of the Princeton Ocean Model. The numerical model and laboratory data agree to within the error of the experiments. The variation with Rossby number, however, is not as great in the numerical model data, for which the exponent is  $0.17 \pm 0.02$ .

#### 4. Summary and conclusions

Laboratory experiments were carried out on a rotating table to simulate a coastal river inflow. Buoyant fluid was introduced perpendicular to the straight tank wall and the density and velocity fields of the evolving plume were measured. The goal of the experiments was to examine the dynamics of the bulge region near the inflow and the effect of the bulge on the alongshore transport in the plume.

The bulge circulation is observed to consist of a growing region of anticyclonic circulation whose momentum is in gradient–wind balance. Fluid discharged from the bulge forms a coastal current along the wall, which is shown to be in geostrophic balance. Direct measurements of the alongshore transport of buoyant fluid in the coastal current show that it is reduced to between 40% and 60% of the inflow discharge. Further, the transport varies inversely with the inflow Rossby number.

In contrast to previous studies, which have sought to characterize the bulge by a single horizontal length scale, two scales are found to determine the behaviour of the bulge. The displacement of the bulge centre away from the wall is set by the inflow momentum and scales with the inertial radius  $L_i$ . The effective radius of the bulge based on its total area scales with the bulge Rossby radius  $L_b$ . The ratio of these two scales,  $L^*$ , determines the behaviour of the bulge. When  $L^*$  is small, the bulge is held close to the wall and a large fraction of the inflowing fluid is forced out of the bulge and into the coastal current. As  $L^*$  increases, the bulge moves further from the wall and a smaller fraction of fluid is discharged into the coastal current. When  $L^*$  is large, the bulge becomes unstable, alternately separating from and reattaching to the wall and causing the flow in the coastal current to be pulsed.

Using the above scales, the reduction in alongshore transport due to the bulge growth is expected to depend on the inflow Rossby number according to  $Ro^{1/4}$ . This is consistent with the bulge growth rates inferred from coastal current transport measurements which vary as  $Ro^{0.32 \pm 0.18}$ . Numerical modelling experiments spanning a larger range for  $Ro$  have a smaller power dependence on the Rossby number (although within the error bounds of the laboratory data fit), suggesting that it is likely that the scaling for the bulge area is more complex than the simple product of scales  $L_i L_b$  and perhaps deviates from the 1/4 power law associated with this scaling. Nevertheless, the consistency between the simple theory and experimental data is encouraging and emphasizes the importance of the two scales in setting the transport of plume water.

The present experiments focus on the initiation and evolution of the plume circulation in the first 1–10 days. While natural river plumes are not initiated in the same fashion as the laboratory experiments, they are routinely reset owing to changes in ambient forcing such as wind, which occur on the same time scale as the experiments (Hickey *et al.* 1998). In naturally occurring plumes, however, remaining buoyant fluid may play an important role in the evolution of a rebuilding river plume after such an event. The stratification and frontal structure resulting from the remaining fluid will support internal waves and other dynamics not included in the present study. Future work that takes these dynamics into account will increase both the complexity and the realism of the conceptual model of plume evolution presented here.

We thank Jeffrey Koseff for support and helpful discussions and Todd Cowen for graciously providing his PIV codes. We would also like to thank the anonymous reviewers who helped streamline and improve the manuscript. This research was supported by NSF grant OCE-0118029.

### Appendix. Experimental parameters

---

| Run  | $T$ | $Q$                         | $g'$               | $W$ | $H$ | $Ro$ | $Fr$ |
|------|-----|-----------------------------|--------------------|-----|-----|------|------|
| —    | s   | $\text{cm}^3 \text{s}^{-1}$ | $\text{cm s}^{-2}$ | cm  | cm  | —    | —    |
| FF1  | 20  | 10.6                        | 6.9                | 5   | 1   | 0.67 | 0.81 |
| FF2  | 20  | 10.6                        | 6.9                | 5   | 1   | 0.67 | 0.81 |
| HB1  | 20  | 10.6                        | 6.9                | 5   | 1   | 0.67 | 0.81 |
| HB2  | 20  | 10.6                        | 6.9                | 5   | 1   | 0.67 | 0.81 |
| HB3  | 23  | 10.6                        | 6.9                | 5   | 1   | 0.78 | 0.81 |
| HB4  | 25  | 10.6                        | 6.9                | 5   | 1   | 0.84 | 0.81 |
| HB5  | 28  | 10.6                        | 6.9                | 5   | 1   | 0.94 | 0.81 |
| HB6  | 15  | 10.6                        | 6.9                | 5   | 1   | 0.51 | 0.81 |
| HB7  | 30  | 10.6                        | 6.9                | 5   | 1   | 1.00 | 0.81 |
| HB8  | 35  | 10.6                        | 6.9                | 5   | 1   | 1.20 | 0.81 |
| HB9  | 40  | 10.6                        | 6.9                | 5   | 1   | 1.30 | 0.81 |
| HB10 | 25  | 14.8                        | 6.9                | 5   | 1   | 1.20 | 1.10 |
| HB11 | 25  | 10.6                        | 6.9                | 5   | 1   | 0.84 | 0.81 |
| HB12 | 20  | 10.6                        | 6.9                | 5   | 1   | 0.67 | 0.81 |
| HB13 | 20  | 7.1                         | 6.9                | 5   | 1   | 0.45 | 0.54 |
| HB14 | 20  | 7.1                         | 6.9                | 5   | 1   | 0.45 | 0.54 |
| HB15 | 35  | 7.1                         | 6.9                | 5   | 1   | 0.79 | 0.54 |
| HB16 | 25  | 10.6                        | 14                 | 5   | 1   | 0.84 | 0.57 |
| HB17 | 25  | 10.6                        | 14                 | 2.5 | 1   | 3.40 | 1.10 |
| HB18 | 25  | 9.8                         | 3.5                | 5   | 1   | 0.78 | 1.00 |
| HB19 | 20  | 9.8                         | 3.5                | 5   | 1   | 0.62 | 1.00 |
| HB20 | 35  | 9.8                         | 3.5                | 5   | 1   | 1.10 | 1.00 |
| HB21 | 10  | 10.6                        | 6.9                | 5   | 1   | 0.34 | 0.81 |
| HB22 | 20  | 16.7                        | 6.9                | 5   | 1   | 1.06 | 1.26 |
| HB23 | 25  | 16.7                        | 6.9                | 5   | 1   | 1.32 | 1.26 |
| HB24 | 25  | 2.9                         | 3.5                | 5   | 1   | 0.23 | 0.31 |

---

TABLE 1. Experimental parameters for the horizontal sheet bulge runs.

---

| Run  | $T$ | $Q$                         | $g'$               | $W$ | $H$ | $Ro$ | $Fr$ |
|------|-----|-----------------------------|--------------------|-----|-----|------|------|
| —    | s   | $\text{cm}^3 \text{s}^{-1}$ | $\text{cm s}^{-2}$ | cm  | cm  | —    | —    |
| VB1  | 25  | 9.8                         | 7                  | 5   | 1   | 0.78 | 0.74 |
| VB2  | 20  | 9.8                         | 7                  | 5   | 1   | 0.62 | 0.74 |
| VB3  | 25  | 6.4                         | 7                  | 5   | 1   | 0.51 | 0.48 |
| VB4  | 40  | 9.8                         | 7                  | 5   | 1   | 1.25 | 0.74 |
| VB5  | 25  | 16.0                        | 7                  | 5   | 1   | 1.27 | 1.21 |
| VB6  | 30  | 8.9                         | 7                  | 5   | 1   | 0.84 | 0.67 |
| VB7  | 24  | 9.8                         | 3.5                | 5   | 1   | 0.78 | 1.05 |
| VB8  | 20  | 9.8                         | 3.5                | 5   | 1   | 0.62 | 1.05 |
| VB9  | 25  | 6.4                         | 3.5                | 5   | 1   | 0.51 | 0.68 |
| VB10 | 40  | 9.8                         | 3.5                | 5   | 1   | 1.25 | 1.05 |
| VB11 | 25  | 16.0                        | 3.5                | 5   | 1   | 1.27 | 1.7  |
| VB12 | 25  | 9.8                         | 14                 | 5   | 1   | 0.78 | 0.52 |

TABLE 2. Experimental parameters for bulge depth runs.

---

| Run  | $T$ | $Q$                         | $\theta_i$ | $g'$               | $W$ | $H$ | $Ro$ | $Fr$ |
|------|-----|-----------------------------|------------|--------------------|-----|-----|------|------|
| —    | s   | $\text{cm}^3 \text{s}^{-1}$ | deg.       | $\text{cm s}^{-2}$ | cm  | cm  | —    | —    |
| CC1  | 20  | 9.8                         | 90         | 7                  | 5   | 1   | 0.62 | 0.74 |
| CC2  | 35  | 9.8                         | 90         | 7                  | 5   | 1   | 1.1  | 0.74 |
| CC3  | 15  | 9.8                         | 90         | 7                  | 5   | 1   | 0.47 | 0.74 |
| CC4  | 30  | 9.8                         | 90         | 7                  | 5   | 1   | 0.94 | 0.74 |
| CC5  | 25  | 9.8                         | 90         | 7                  | 5   | 1   | 0.78 | 0.74 |
| CC6  | 40  | 9.8                         | 90         | 7                  | 5   | 1   | 1.20 | 0.74 |
| CC7  | 25  | 6.4                         | 90         | 7                  | 5   | 1   | 0.51 | 0.48 |
| CC8  | 25  | 13.2                        | 90         | 7                  | 5   | 1   | 1.10 | 1.00 |
| CC9  | 25  | 8.1                         | 90         | 7                  | 5   | 1   | 0.64 | 0.61 |
| CC10 | 25  | 11.5                        | 90         | 7                  | 5   | 1   | 0.92 | 0.87 |
| CC11 | 25  | 9.8                         | 90         | 7                  | 5   | 1   | 0.78 | 0.74 |
| CC12 | 25  | 2.9                         | 90         | 7                  | 5   | 1   | 0.23 | 0.22 |
| CC13 | 25  | 16.2                        | 90         | 7                  | 5   | 1   | 1.30 | 1.20 |
| CC14 | 15  | 6.4                         | 90         | 7                  | 5   | 1   | 0.31 | 0.48 |
| CC15 | 25  | 9.8                         | 90         | 7                  | 2.5 | 1   | 3.10 | 1.50 |
| CC16 | 35  | 6.4                         | 90         | 7                  | 2.5 | 1   | 2.9  | 0.97 |
| CC17 | 15  | 11.5                        | 90         | 7                  | 5   | 1   | 0.55 | 0.87 |
| CC18 | 25  | 9.8                         | 90         | 3.5                | 5   | 1   | 0.78 | 1.00 |
| CC19 | 25  | 6.4                         | 90         | 3.5                | 5   | 1   | 0.51 | 0.68 |
| CC20 | 25  | 13.2                        | 90         | 3.5                | 5   | 1   | 1.10 | 1.40 |
| CC21 | 30  | 2.9                         | 90         | 3.5                | 5   | 1   | 0.28 | 0.31 |
| CC22 | 15  | 9.8                         | 90         | 3.5                | 5   | 1   | 0.47 | 1.00 |
| CC23 | 35  | 9.8                         | 90         | 3.5                | 5   | 1   | 1.10 | 1.00 |
| CC24 | 15  | 13.2                        | 90         | 3.5                | 5   | 1   | 0.63 | 1.40 |

TABLE 3. Experimental parameters for coastal current transport runs.

## REFERENCES

- AVICOLA, G. & HUQ, P. 2002 Scaling analysis for the interaction between a buoyant coastal current and the continental shelf: experiments and observations. *J. Phys. Oceanogr.* **32**, 3233–3248.
- AVICOLA, G. & HUQ, P. 2003a The characteristics of the recirculating bulge region in coastal buoyant outflows. *J. Mar. Res.* **61**, 435–463.
- AVICOLA, G. & HUQ, P. 2003b The role of outflow geometry in the formation of the recirculating bulge region in coastal buoyant outflows. *J. Mar. Res.* **61**, 411–434.

- BORMANS, M. & GARRETT, C. 1989 A simple criterion for gyre formation by the surface outflow from a strait, with application to the Alboran Sea. *J. Geophys. Res.* **94**(C9), 12 637–12 644.
- CHAO, S.-Y. & BOICOURT, B. 1986 Onset of estuary plumes. *J. Phys. Oceanogr.* **16**, 2137–2149.
- COLON, D. M. 1983 On the outflow modes of the Tsugaru warm current. *La Mer* **20**, 60–64.
- COWEN, E. A., CHANG, K.-A. & LIAO, Q. 2001 A single camera coupled PTV-LIF technique. *Exps. Fluids* **31**, 63–73.
- CRIMALDI, J. P. & KOSEFF, J. R. 2001 High-resolution measurements of the spatial and temporal structure of a turbulent plume. *Exps. Fluids* **31**, 90–102.
- FONG, D. A. 1998 Dynamics of freshwater plumes: observations and numerical modelling of the wind-forced response and alongshore freshwater transport. PhD thesis, Woods Hole Oceanographic Institute/Massachusetts Institute of Technology.
- FONG, D. A. & GEYER, W. R. 2002 The alongshore transport of fresh water in a surface-trapped river plume. *J. Phys. Oceanogr.* **32**, 957–972.
- GARVINE, R. W. 1995 A dynamical system for classifying buoyant coastal discharges. *Cont. Shelf Res.* **15**, 1585–1596.
- GARVINE, R. W. 1999 Penetration of buoyant coastal discharge onto the continental shelf: a numerical model experiment. *J. Geophys. Res.* **29**, 1892–1909.
- GARVINE, R. W. 2001 The impact of model configuration in studies of buoyant coastal discharge. *J. Mar. Res.* **59**, 193–225.
- GILL, A. E. 1982 *Atmosphere–Ocean Dynamics*. Academic.
- GLEIZON, P., CHABERT D’HIERES, G. & RENOARD, D. 1996 Experimental study of the Alboran Sea gyres. *Oceanol. Acta* **19**, 499–511.
- GRIFFITHS, R. W. & HOPFINGER, E. J. 1983 Gravity currents moving along a lateral boundary in a rotating fluid. *J. Fluid Mech.* **134**, 357–399.
- HICKEY, B. M., PEITRAFESA, L. J., JAY, D. A. & BOICOURT, W. C. 1998 The Columbia River plume study: subtidal variability in the velocity and salinity field. *J. Geophys. Res.* **103**(C5), 10 339–10 368.
- HOLTON, J. R. 1972 *An Introduction to Dynamic Meteorology*. Academic.
- HORNER, A. R., FONG, D. A., KOSEFF, J. R., MAXWORTHY, T. & MONISMITH, S. G. 2000 The control of coastal current transport. *Fifth International Symposium on Stratified Flows*, vol. 2, pp. 865–870. International Association of Hydraulic Research.
- HORNER-DEVINE, A. R. 2003 The dynamics of buoyant, rotational river plumes. PhD thesis, Stanford University.
- KAWASAKI, Y. & SUGIMOTO, T. 1984 Experimental studies on the formation and degeneration processes of the Tsugaru Warm Gyre. *Ocean Hydrodynamics of the Japan and East China Seas* (ed. Ichiye, T., pp. 225–238). Elsevier.
- KLINGER, B. A. 1994 Baroclinic eddy generation at a sharp corner in a rotating system. *J. Geophys. Res.* **99** (C6) 12 515–12 531.
- KOURAFALOU, V. H., OEY, L. Y., WANG, J. D. & LEE, T. N. 1996 The fate of river discharge on the continental shelf: Part 1. Modeling the river plume and the inner shelf coastal current. *J. Geophys. Res.* **101**(C2), 3415–3434.
- LANOIX, F. 1974 Projet Alboran. Etude hydrologique et dynamique de la mer d’Alboran. *Rapp. Tech. OTAN*, **66**, 39–50.
- LENTZ, S. J. & HELFRICH, K. R. 2002 Buoyant gravity currents along a sloping bottom in a rotating fluid. *J. Fluid Mech.* **464**, 251–278.
- MASSE, A. K. & MURTHY, C. R. 1992 Analysis of the Niagra River Plume. *J. Geophys. Res.* **97**(C2), 2403–2420.
- NOF, D. 1988 Eddy–wall interaction. *J. Mar. Res.* **46** (C6) 527–555.
- NOF, D. & PICHEVIN, T. 2001 The ballooning of outflows. *J. Phys. Oceanogr.* **31**, 3045–3058.
- OEY, L. Y. & MELLOR, G. L. 1993 Subtidal variability of estuarine outflow, plume and coastal current: a model study. *J. Phys. Oceanogr.* **23**, 164–171.
- SADOUX, S., BAEY, J.-M., FINCHAM, A. & RENOARD, D. 2000 Experimental study of the stability of an intermediate current and its interaction with a cape. *Dyn. Atmos. Ocean* **31**, 165–192.
- STERN, M. E., WHITEHEAD, J. A. & HUA, B.-L. 1982 The intrusion of a density current along the coast of a rotating fluid. *J. Fluid Mech.* **123**, 237–265.

- WHITEHEAD, J. A. 1985 The deflection of a baroclinic jet by a wall in a rotating fluid. *J. Fluid Mech.* **157**, 79–93.
- WHITEHEAD, J. A. & CHAPMAN, D. C. 1986 Laboratory observations of a gravity current on a sloping bottom: the generation of shelf waves. *J. Fluid Mech.* **172**, 373–399.
- WHITEHEAD, J. A. & MILLER, A. R. 1979 Laboratory simulation of the gyre in the Alboran Sea. *J. Geophys. Res.* **84**, 3733–3742.
- YANKOVSKY, A. E. & CHAPMAN, D. C. 1997 A simple theory for the fate of buoyant coastal discharges. *J. Phys. Oceanogr.* **27**, 1386–1401.